Experimental photonic quantum memristor

Experimental photonic quantum memristor

Michele Spagnolo,[1] Joshua Morris,[1] Simone Piacentini,[2,3] Michael Antesberger,[1] Francesco
Massa,[1] Andrea Crespi,[2,3] Francesco Ceccarelli,[3,2] Roberto Osellame,[3,2] and Philip Walther[1,4]

[1]University of Vienna, Faculty of Physics, Vienna Center for Quantum Science and Technology (VCQ), 1090 Vienna, Austria
[2]Dipartimento di Fisica, Politecnico di Milano, piazza L. Da Vinci 32, 20133 Milano, Italy
[3]Istituto di Fotonica e Nanotecnologie, Consiglio Nazionale delle Ricerche (IFN-CNR), piazza L. Da Vinci 32, 20133 Milano, Italy
[4]Christian Doppler Laboratory for Photonic Quantum Computer,
Faculty of Physics, University of Vienna, 1090 Vienna, Austria

SUPPLEMENTARY INFORMATION

A. Output state of the quantum memristor

Let us rewrite for convenience the input state

$$|\psi_{\text{in}}(t)\rangle = \alpha(t)\,|0\rangle_A + \beta(t)\,|1\rangle_A. \quad (5)$$

When going through a beam splitter with reflectivity $R(t)$ the state evolves into:

$$
\begin{aligned}
|\psi_{\text{out,CD}}(t)\rangle = &\; \alpha(t)\,|0\rangle_C\,|0\rangle_D + \\
&+ \beta(t)\sqrt{1-R(t)}\,|1\rangle_C\,|0\rangle_D + \\
&+ i\beta(t)\sqrt{R(t)}\,|0\rangle_C\,|1\rangle_D, \quad (11)
\end{aligned}
$$

which corresponds to the following density matrix (let us omit the time t and the subscripts C and D for ease of reading):

$$
\begin{aligned}
\rho_{\text{out,CD}} = |\psi_{\text{out,CD}}\rangle\langle\psi_{\text{out,CD}}| = &\; |\alpha|^2\,|00\rangle\langle00| + \\
+ \alpha\beta^*\sqrt{1-R}\,|00\rangle\langle10| &- i\alpha\beta^*\sqrt{R}\,|00\rangle\langle01| + \\
+ \alpha^*\beta\sqrt{1-R}\,|10\rangle\langle00| &+ |\beta|^2(1-R)\,|10\rangle\langle10| + \\
- i|\beta|^2\sqrt{R(1-R)}\,|10\rangle\langle01| &+ i\alpha^*\beta\sqrt{R}\,|01\rangle\langle00| + \\
+ i|\beta|^2\sqrt{R(1-R)}\,|01\rangle\langle10| &+ |\beta|^2 R\,|01\rangle\langle01|.
\end{aligned}
$$

Note that output D is used for the feedback of the quantum memristor, whereas the user has only access to output C. The output state related to mode C can be obtained from the previous density matrix by taking the partial trace over D, and results in:

$$
\begin{aligned}
\rho_{\text{out,C}} = \text{Tr}_D(\rho_{\text{out,CD}}) = &\; |\alpha|^2\,|0\rangle\langle0|_C + \\
+ \alpha\beta^*\sqrt{1-R}\,|0\rangle\langle1|_C &+ \alpha^*\beta\sqrt{1-R}\,|1\rangle\langle0|_C + \\
+ |\beta|^2(1-R)\,|1\rangle\langle1|_C &+ |\beta|^2 R\,|0\rangle\langle0|_C, \quad (12)
\end{aligned}
$$

which is equal to the one shown in Eq. (7). In the matrix representation for the basis $|0\rangle_C, |1\rangle_C$ this state corresponds to:

$$
\rho_{\text{out,C}} = \begin{pmatrix} |\alpha|^2 + |\beta|^2 R & \alpha^*\beta\sqrt{1-R} \\ \alpha\beta^*\sqrt{1-R} & |\beta|^2(1-R) \end{pmatrix} \quad (13)
$$

from which the purity is given by

$$\text{Tr}\big(\rho_{\text{out,C}}{}^2(t)\big) = 1 - 2|\beta|^4 R(1-R), \quad (8)$$

B. Converting photon-number encoding to path-encoding.

In Supplementary Information A we have developed the theory of the quantum memristor with an encoding scheme where the qubit is represented by a superposition of Fock states, also known as single-rail encoding. In a path-encoded picture (also known as dual-rail) the qubit is represented instead by a single photon being in a superposition of two spatial modes. The $|0\rangle$ state corresponds to the photon being in one mode, say mode A, and the $|1\rangle$ state corresponds to the photon being in the other mode, say mode B. In short, the map from number encoding to path encoding is the following:

$$
\begin{aligned}
|0\rangle_A &\rightarrow |1\rangle_A\,|0\rangle_B \quad (14) \\
|1\rangle_A &\rightarrow |0\rangle_A\,|1\rangle_B \quad (15)
\end{aligned}
$$

so our equivalent input state will be

$$|\psi_{\text{in}}(t)\rangle = \alpha(t)\,|1\rangle_A\,|0\rangle_B + \beta(t)\,|0\rangle_A\,|1\rangle_B. \quad (16)$$

By looking at Eq. (11) it is evident that the $|0\rangle_A$ state is not affected by the beam splitter, which only acts on the $|1\rangle_A$ state. As a result, the dual-rail equivalent should be one where mode A goes directly to the output, whereas mode B goes into the tunable beam splitter (or its integrated equivalent, i.e. a tunable Mach-Zehnder). This is precisely the scheme shown in Fig. 2d. By evolving the input state through the Mach-Zehnder we obtain

$$
\begin{aligned}
|\psi_{\text{out,ABC}}(t)\rangle = &\; \alpha(t)\,|1\rangle_A\,|0\rangle_B\,|0\rangle_C + \\
&+ \beta(t)\sqrt{1-R(t)}\,|0\rangle_A\,|1\rangle_B\,|0\rangle_C + \\
&+ i\beta(t)\sqrt{R(t)}\,|0\rangle_A\,|0\rangle_B\,|1\rangle_C, \quad (17)
\end{aligned}
$$

which is the dual-rail equivalent of Eq. (11). The output mode C is used as measurement port for updating the state of the quantum memristor, whereas the user only has access to the output modes A and B. In order to obtain the output states of modes A and B, one has to write $|\psi_{\text{out,ABC}}(t)\rangle$ in terms of density matrix and then take the partial trace over C. With similar calculations to the ones presented in the previous paragraph, one obtains the following density matrix

$$
\rho_{\text{out,AB}} = \begin{pmatrix} |\beta|^2 R & 0 & 0 \\ 0 & |\alpha|^2 & \alpha^*\beta\sqrt{1-R} \\ 0 & \alpha\beta^*\sqrt{1-R} & |\beta|^2(1-R) \end{pmatrix} \quad (18)
$$

(written in the basis $|00\rangle_{\text{AB}}, |01\rangle_{\text{AB}}, |10\rangle_{\text{AB}}$). We can straightforwardly obtain the purity

$$\text{Tr}\big(\rho_{\text{out,AB}}^2(t)\big) = 1 - 2|\beta|^4 R(1-R), \qquad (19)$$

which is the same as in Eq. (8). As in the single-rail case, we take $\langle n_{\text{in}}\rangle$ and $\langle n_{\text{out}}\rangle$ to represent the number of photons going in and out of the Mach-Zehnder and this corresponds to $\langle n_{\text{in}}(t)\rangle = |\beta(t)|^2$, $\langle n\rangle_{\text{max}} = 1$ and $\langle n_{\text{out}}(t)\rangle = |\beta(t)|^2\big[1 - R(t)\big] = \big[1 - R(t)\big]\langle n_{\text{in}}(t)\rangle$. This shows for the quantum memristor that the two pictures are perfectly equivalent.

The advantage of having switched to dual-rail encoding is, unlike the single-rail encoding, the straightforward manipulation of the qubit. In fact, any arbitrary state of the form of Eq. (16) can be generated by a Mach-Zehnder interferometer with a tunable phase shifters in one of the output arms. This configuration was used as preparation stage for the quantum memristor, and a similar configuration as a final tomography stage after the quantum memristor for choosing arbitrary measurment basis enabling the reconstruction of the density matrix of the output state (see Fig. 2e). This tomography stage was only used for characterization purposes and otherwise set to perform an identity operation.

C. Fabrication of the integrated photonic quantum processor

The fabrication of the integrated photonic chip is based on the femtosecond laser micromachining process [1]. Single-mode optical waveguides, optimised for operation at 1550 nm, are inscribed in a alumino-borosilicate glass (Corning EAGLE XG, 1.1 mm thick) by focusing laser pulses (Yb:KYW cavity-dumped mode-locked laser: 1030 nm wavelength, 300 fs pulse duration, 520 nJ energy per pulse, 1 MHz repetition rate) with a $50\times$ objective (0.65 NA) equipped with an aberration-correction collar. The entire optical circuit is inscribed at 25 μm from the bottom surface of the substrate, by translating the substrate at the constant speed of 40 mm/s. In particular, six overlapped laser scans are performed along the desired waveguide path. In order to obtain single-mode operation and reduce the waveguide birefringence [2], the inscription process is followed by a thermal annealing composed of a fast rising ramp of 12 °C/min up to 750 °C and by two subsequent slow falling ramps of 12 °C/h and 24 °C/h, respectively down to 630 °C and 500 °C. After that, the cooling process is completed with no control on the temperature ramps. At the end of the waveguide fabrication process, the measured insertion loss is 1.2 dB, corresponding to a transmission of 76%. Each Mach-Zehnder interferometer is composed of two balanced directional couplers (zero interaction length and 7.5 μm coupling distance), that are connected to the rest of the circuit by S-bend waveguides (40 mm curvature radius) and by straight waveguides (separation $p = 127$ μm and length $L = 2$ mm).

In order to guarantee maximum efficiency and minimal crosstalk of the phase shifting operation, thermal insulating trenches are ablated at both sides of the optical waveguides that are supposed to be phase-tuned. To fabricate the trenches we used laser pulses (Light Conversion PHAROS: 1030 nm wavelength, 1 ps pulse duration, 1.5 μJ energy per pulse, 20 kHz repetition rate) focused by a $20\times$ water-immersion objective (0.50 NA) on the bottom surface of the substrate, while the latter is translated at 4 mm/s entirely immersed in distilled water. This fabrication technique is usually referred to as water-assisted laser ablation [3, 4]. In order to realise a single trench with depth $D_t = 300$ μm, width $W_t = 97$ μm and length $L_t = L = 2$ mm, four rectangular glass blocks (depth $D_b = D_t/4 = 75$ μm) are removed one after the other by ablating only the perimeter of each block and making it detach and fall into the water. In this way, deep trenches are fabricated on the bottom side of the substrate with near-unity yield.

After that, the substrate is flipped and the process continues on the bottom side with the fabrication of the thermal phase shifters [5]. Firstly, after a standard piranha cleaning bath, a metal multilayer film, composed of 3 nm of chromium and 100 nm of gold, is deposited on the entire area of the chip by using a magnetron sputtering system. Secondly, a further thermal annealing (rising ramp of 10 °C/min up to 500 °C, followed by 60 min at this temperature and by a cooling process with no thermal actuation) is employed to reach a stable value of the electrical resistivity and to prevent electrical drifts that would impair the stability of the phase shifting operation. Lastly, the thermal phase shifters are patterned by laser pulses (Yb:KYW cavity-dumped mode-locked laser: 1030 nm wavelength, 300 fs pulse duration, 200 nJ energy per pulse, 1 MHz repetition rate) focused on the chip surface with a $10\times$ objective (0.25 NA). By translating the substrate at 2 mm/s, contact pads and electrodes are isolated by selectively removing the metal. Resistive microheaters having width $W_r = p - W_t = 30$ μm and length $L_r = L = 2$ mm are instead isolated by the presence of the trenches. The average electrical resistance of the microheaters is 38 Ω, while the resulting electrical power needed to induce a 2π phase shift is as low as 55 mW.

In the end, the photonic chip is mounted on an aluminium heat sink, wire-bonded to a printed circuit board and pigtailed to both input and output single-mode optical fibers. After the pigtailing process, the total insertion loss from input to output fibers is 2 dB, corresponding to a transmission of 63%.

D. Implementation of the feedback law for the quantum memristor

The general solution of Eq. (4) is

$$R(t) = c + \int_0^t \left(\langle n_{\text{in}}(\tau)\rangle - 0.5\right) d\tau. \qquad (20)$$

where we assumed $\langle n\rangle_{\text{max}} = 1$ and c an arbitrary constant. In our case we want to set $c = 0.5$ in order to restore the baseline of R to zero.

Even more importantly, we must make sure that in all cases $R(t)$ remains bound in the interval $[0, 1]$. This means that a saturation mechanism must be introduced so that the integral does not diverge when $\langle n_{\text{in}}(t)\rangle$ is constant or slowly varying. The most physically meaningful way to do so is to integrate over a sliding time window of width T, which can be written

as

$$R(t) = 0.5 + \frac{1}{T} \int_{t-T}^{t} \left(\langle n_{\text{in}}(\tau) \rangle - 0.5 \right) d\tau. \qquad (9)$$

In other words, at every given time t the memristor "forgets" what happened before time $t - T$.

The resulting dynamics of our device can be tested by assuming, for example, a periodic input of the form $\langle n_{\text{in}}(t) \rangle = \sin^2(\pi/T_{\text{osc}}\, t)$. Depending on the relation between the oscillation period of the input, T_{osc}, and the integration time, T, two limiting regimes can already be identified. When $T_{\text{osc}} \gg T$, i.e. the input is (almost) constant, Eq. (9) reduces to $R(t) = \langle n_{\text{in}} \rangle$, which inserted into Eq. (3) gives

$$\langle n_{\text{out}} \rangle_{\text{LF}} = \langle n_{\text{in}} \rangle - \langle n_{\text{in}} \rangle^2. \qquad (21)$$

In contrast, when the input oscillates very quickly such that $T_{\text{osc}} \ll T$, the integral tends to zero, so that $R(t) = 0.5$ and consequently

$$\langle n_{\text{out}} \rangle_{\text{HF}} = 0.5 \langle n_{\text{in}} \rangle. \qquad (22)$$

Note that when $T = T_{\text{osc}}$ the integral is zero, as we are integrating over a full period. Hence, integrating over more than one period yields redundant results. For this reason, in the main text we show examples with integration times only in the range of one period.

Finally, we emphasize that, according to Chua's own definition [6], a memristive device is indistinguishable from a nonlinear resistor at very low frequencies, and reduces to a linear resistor at high frequencies. This is exactly the case of our photonic quantum memristor, as shown in Eq. (21) and (22).

For the practical implementation of Eq. (9) we discuss how the feedback loop retrieves $\langle n_{\text{in}} \rangle$. This is straightforward, as the input is linked to the measurement in port D by $\langle n_{\text{in}} \rangle = \langle n_{\text{meas,D}} \rangle / R$ (see Fig. 2a). In practice, we use a microcontroller that samples $\langle n_{\text{meas,D}} \rangle$, estimates $\langle n_{\text{in}} \rangle$ using the previous value of $R(t)$, performs the integral and consequently updates the value of $R(t')$. This operation is executed at a sampling rate of approximately 20 kSa/s. A control is implemented in the code that prevents $R(t)$ from going exactly to zero, otherwise the feedback would break.

E. Experimental setup

The experimental setup used for our demonstration is detailed in Fig. 6. A collinear Type II SPDC source emits pairs of identical photons at 1550 nm. The source is based on a 30 mm PPKTP crystal with a poling period of 46.2 µm adapted for downconversion from 775 to 1550 nm. The crystal is pumped by a CW amplified diode laser (Toptica TA Pro 780) with a pump power of approximately 80 mW. The crystal is inserted in a Sagnac interferometer which produces polarisation-entangled photons, although in this specific case the entanglement is not used.

One of the photons (idler) is sent directly to the detectors for heralding, while the other (signal) is coupled to the integrated photonic processor via a single-mode fiber which is directly glued to its surface. In the photonic processor, the photon goes through the state preparation stage and then through the quantum memristor. At the output, the processor is pigtailed to single-mode fibers attached to the detectors. We use superconducting nanowire single-photon detectors (PhotonSpot Inc.) with average detection efficiency above 95%. We use three detectors: one for the heralding (idler) photon, one for the feedback signal, and one for the output signal.

After the detectors, a logic unit analyses the signals. Every idler-feedback coincidence triggers the generation of a square voltage pulse in the feedback channel. Equally, every idler-output coincidence triggers a voltage pulse in the output channel. With a pump power of about 80 mW in the source, the maximum coincidence rate in each channel is approximately 3×10^4 counts/s. Both channels are then low-pass filtered with $RC = 100$ ms filters. This has the effect of averaging the trains of pulses and providing a continuous voltage signal that is proportional to the pulse rate, which is in turn proportional to the photon number. Measuring the output voltage of the RC filters constitutes therefore a measurement of the photon number expectation value. Note that, following the discussion around Eq. (9) in the main text, the time constant RC should be much smaller than the integration time T, which is clearly the case as we used $T = 10$ s.

At this point, the output signal goes to an oscilloscope for final data logging, while the feedback signal goes to a microcontroller which computes $\langle n_{\text{in}} \rangle$ and uses it to update the new value of $R(t)$ in the chip.

The system is then tested by varying the input number of photon as a sine wave. This is performed by a function generator which acts on the the integrated quantum state preparation stage.

F. Memristive behaviour arising from the phase shifters

The step response of the phase shifters in our chip is reported in Fig. 7. The curve is well approximated by a low-pass filter with a cutoff frequency of $f_{\text{cut}} = 4.62$ Hz. If the memristor operates at frequencies $f_{\text{osc}} \ll f_{\text{cut}}$ the effect of the shifters is negligible. However, when approaching f_{cut} the dynamics of the shifters starts to interfere with the dynamics of the feedback loop. To test the sole effect of the shifters, we set here our microcontroller to implement the identity $R(\theta) = \langle n_{\text{in}} \rangle$, rather than Eq. (4). At this point the dynamics of the device is only governed by how quickly the phase shifter can actually reach the value $R(\theta)$ set by the microcontroller.

The resulting hysteresis figure, which we report in Fig. 8, is very similar to the one we obtained by implementing the windowed integrator (see Supplementary Information D). This is not surprising, considering that a low-pass filter and a windowed integrator converge to the same limits both at low and high frequencies. Furthermore, this result indicates another viable path for the future development of these devices, where one could engineer the response of the thermal shifters to further simplify the quantum memristor layout by removing some components in the feedback signal processing.
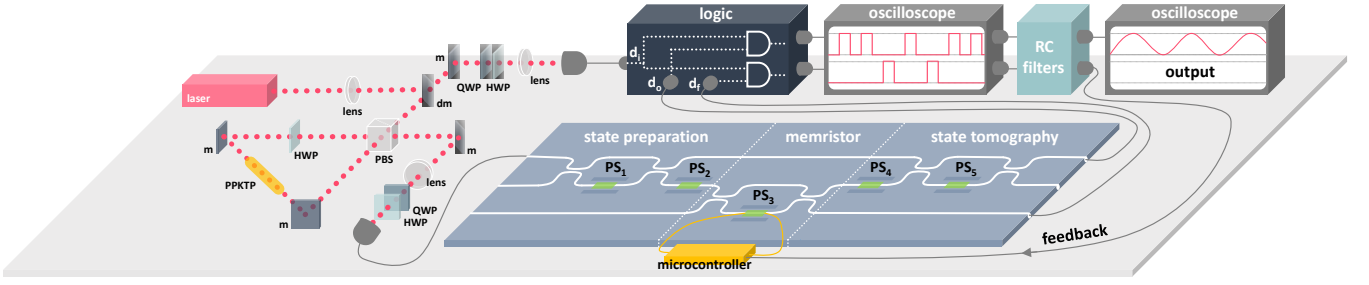
Figure 6. **Experimental setup.** Pumped by a continuous wave laser, a spontaneous parametric downconversion source using periodically-poled KTP crystal (PPKTP) generates orthogonally polarised photon pairs with a wavelength of 1550 nm. By using a polarization beamsplitter (PBS) the photon pairs are separated such that the measurement of one photon heralds the presence of the other photon that is coupled into the photonic quantum memristor processor. The state preparation stage, consisting of a Mach-Zehnder interferometer with two tunable phase shifters (PS) allows for the preparation of the input state for the quantum memristor. In the final part of the device, the photon undergoes a tomography stage, which is used for characterisation purpose and otherwise set to perform an identity transformation. A logic unit analyses the coincidences between the idler photon and the output and feedback photons from the outputs of the photonic processor, triggering the emission of square pulses each time a coincidence is detected. By low-pass-filtering each channel with RC filters we obtain a measurement of photon number both for the output and the feedback signals.
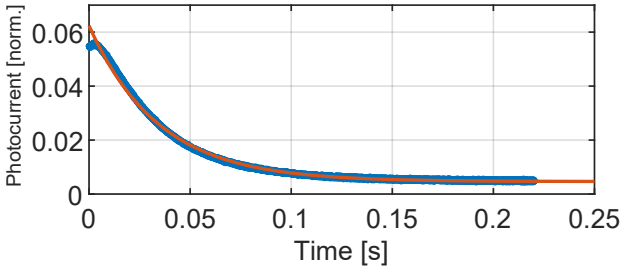

Figure 7. **Step response of the phase shifters.** Specifically, this shows the response of PS3 (see Fig. 2). We inject light in mode B and monitor the output power in mode C with a photodiode. When no voltage is applied to the phase shifter, the Mach-Zehnder is in cross state. When applying a step of $V_{\text{bar}} = 1.145$ V, the Mach-Zehnder switches to bar state, so the power in port C drops to zero. The resulting curve is well approximated by the step-response of a low-pass filter with cutoff frequency $f_{\text{cut}} = 4.62$ Hz.

G. Experimental reconstruction of the output state's density matrix

The density matrix for the output state of our device was obtained in Supplementary Information B:

$$\rho_{\text{out,AB}} = \begin{pmatrix} |\beta|^2 R & 0 & 0 \\ 0 & |\alpha|^2 & \alpha^*\beta\sqrt{1-R} \\ 0 & \alpha\beta^*\sqrt{1-R} & |\beta|^2(1-R) \end{pmatrix} \quad (18)$$

and is written in the basis $|00\rangle_{\text{AB}}, |01\rangle_{\text{AB}}, |10\rangle_{\text{AB}}$. Our chip features a tomography stage that allows in principle to fully reconstruct the output state at modes A and B (see Fig. 2e). The problem is that detecting photons at modes A and B automatically selects the $|01\rangle_{\text{AB}}$ or $|10\rangle_{\text{AB}}$ states, thus cancelling the $|00\rangle_{\text{AB}}$ term (i.e. the upper-left term of the density matrix). In other words, one cannot use photon detection in A and B to characterise the absence of photons in A and B. However, we know from Eq. (17) that the term $|\beta|^2 R$ corresponds to the fraction of photons going to mode C, that is the measurement port of the quantum memristor, connected

to the feedback loop (see Fig. 2e). Therefore, by temporarily disconnecting the feedback loop, we can use the photon count at output C to estimate $|\beta|^2 R$.

In essence, we first use the tomography stage at modes A and B to reconstruct the submatrix relative to the $|01\rangle_{\text{AB}}$ and $|10\rangle_{\text{AB}}$ terms, i.e. the lower-right 2x2 submatrix, using the maximum-likelihood method. We then use the number of detected photons at output C to estimate the upper-left term, and we obtain the final matrix by rescaling according to the normalisation $\text{Tr}(\rho_{\text{out,AB}}) = 1$.

On a final note, it is worth mentioning that the off-diagonal terms need to include an additional phase term $e^{i(\phi_{\text{MZ}}+\phi_{\text{global}})}$. Here, ϕ_{MZ} is the phase introduced by the Mach-Zehnder, which we know because we are controlling the reflectivity of the Mach-Zehnder, which is $R = \cos^2(\phi_{\text{MZ}}/2)$. On the other hand, ϕ_{global} is the global phase that originates in the chip by the difference in length of paths A and B. This cannot be measured a priori, so we actually retrieve this term by fitting the phase of the off-diagonal terms to our data, obtaining $\phi_{\text{global}} = 5.6$ rad.

Clearly, the output density matrix depends on the specific settings of $|\beta|^2$ and R (α depends on β because of the normalisation $|\alpha|^2 + |\beta|^2 = 1$). We characterised the density matrix for the combinations of $|\beta|^2 = [0, 0.3, 0.7, 1]$ and $R = [0, 0.3, 0.5, 0.7, 1]$. Our results are summarised in Table I.

One may argue that these measurements are performed with the feedback loop of the quantum memristor switched off, i.e. with a static value of R, and wonder in principle weather the time-variation of $R(t)$ introduces additional decoherence which is not accounted for in this tomographical reconstruction. The key to understand this issue is in the time scales. If $R(t)$ varied at a frequency comparable or faster than the photon rate, each subsequent photon would experience a different value of $R(t)$, and the photon statistics collected by the detectors would thus reflect a statistical mixture of different photon states, i.e. we would be introducing decoherence. In this device however, $R(t)$ is updated based on the measurement of an expectation value (see Eq. (4)), which requires
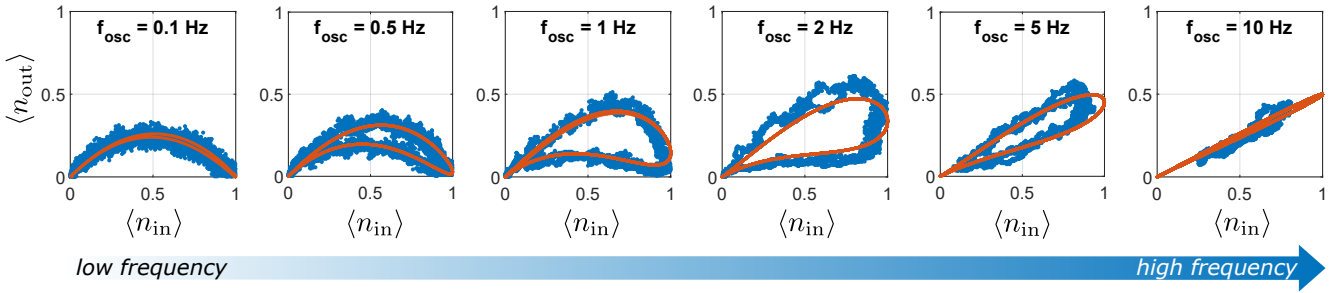
Figure 8. **Memristive behaviour originated by the phase shifters.** Simulations of a feedback loop containing a low-pass filter before the actuation of $R(\theta)$ (red lines) show good agreement with the experimental data (blue lines). The dynamics is very similar to the one we presented in Fig. 3, which is unsurprising considering that low-pass filter and windowed integrator (see Supplementary Information D) have a similar response. The data is more noisy because in this case we work with higher frequencies, so we have to use RC filters (see Supplementary Information E) with $RC = 10$ ms rather than 100 ms. Finally, the reason why at 10 Hz $\langle n_{in} \rangle$ does not cover the full [0,1] range is because the state preparation stage is controlled by an identical phase shifter, which also looses effectiveness when driven around or above its cutoff frequency.

to average over many photon counts, therefore being much slower than the photon rate by definition. In our case, such averaging happens over the characteristic time of a low-pass filter with $RC = 100$ ms, which corresponds to several hundreds photon counts. This represents the fastest time scale at which it would even make sense to update $R(t)$. On top of that, however, the time scale at which the memristor actually updates in our experiment is determined by T (see Eq. (9)), which is two orders of magnitudes larger. Therefore the dynamic operation of the memristor is not introducing any decoherence of the photon states compared to the static reconstruction explained in this paragraph.

H. Quantum reservoir computing

The input to the quantum reservoir is an amplitude-encoded quantum state on a d-dimensional complex Hilbert space. For m modes and p photons, the dimension d grows combinatorially as $\binom{m+p-1}{p}$ with this number giving the maximum dimension of classical input vectors. A classical input vector $\vec{v} \in \mathbb{R}^n$ is continuously encoded into a quantum state q_i as $q_i := \frac{1}{||v||_2} \sum_{j=1}^n v_j |j\rangle$, where $|j\rangle$ is an eigenvector of the computational basis, with $n \leq d$ and v_j the jth element of $\vec{v}$. This state is fed into a beamsplitter matrix with randomly set reflectivity for distributing the coherent quantum information across all modes and subsequently fed into $\lfloor \frac{m}{3} \rfloor$ quantum memristors. The output of each memristor is used as input for another array of beamsplitters that enable a coherent interference after the nonlinear map due to the quantum memristors. We generally assume that the encoding and measurement rails for a quantum memristor do not overlap, thus for M parallel optical memristors one requires $3M$ optical modes. For a full description one could compute the process tensor [7] over the time series length, however it is sufficient for us to consider a list of completely positive trace preserving maps that take the input quantum state and update the next map (dependent on the quantum memristor's state). The first map acts on the initial input state and the measurement outcomes of the quantum memristors adapt the next im-

plementation map that acts on the next input to the reservoir. This is repeated t times, where t is the length of the time sequence for the input data.

The tth output density operator of the quantum reservoir is treated as the correlated output of the reservoir. This final output state is measured via a positive operator-valued measure (POVM) using the Fock basis F, with elements defined as $F_{ij...k} = |ij...k\rangle\langle ij...k|$. A probability vector corresponding to the outcome probabilities of these projectors $\{\mathrm{tr}[\rho_t F_{p00...0}], \mathrm{tr}[\rho_t F_{(p-1)10...0}], \mathrm{tr}[\rho_t F] ..., \mathrm{tr}[\rho_t F_{ij...k}]\} \in \mathbb{R}^d$ serves as the training data for the classical readout network.

Since the statistics of the photon counters are dependent on the quantum memristor's beam splitter settings of the previous iteration, the overall final output vector is correlated with the entire input sequence. In this way, correlations across time are propagated within the quantum reservoir and affect the output probability vector. Note, that the exact input state to the quantum memristors is no longer known, instead the memory effect is implemented as a discrete-time update rule analogous of Eq. (2), but with time steps defined as a set number of channel uses (generally around a thousand photon detection events each). This preserves the memory effect of the quantum memristors and leads to a stateful quantum reservoir that can be exploited for learning tasks both quantum and classical in nature.

The readout network itself is near trivial by design, as we want to ensure any sophisticated estimation is performed by the reservoir. The network exists purely as a linear mapping between the unknown outputs of the quantum reservoir and a human readable classifier. The output probability vector from the quantum reservoir is fed into the input layer and propagated through the network, which contains only a single hidden layer. All neurons except those in the output layer do not have an activation function and thus the neural network implements an entirely linear transform. A softmax function operates on the W neurons of the output layer of the neural

	$\lvert\beta\rvert^2$	R	$\rho_{\text{out,TH}}$	$\rho_{\text{out,EXP}}$	Fidelity [%]	$\text{Tr}\left(\rho_{\text{out,TH}}{}^2\right)$	$\text{Tr}\left(\rho_{\text{out,EXP}}{}^2\right)$
1	0.0	0.0	$\begin{pmatrix} 0.00 & 0 & 0 \\ 0 & 1.00 & -0.00-0.00i \\ 0 & -0.00+0.00i & 0.00 \end{pmatrix}$	$\begin{pmatrix} 0.00 & 0 & 0 \\ 0 & 1.00 & -0.02+0.03i \\ 0 & -0.02-0.03i & 0.00 \end{pmatrix}$	99.62	1.00	0.99
2	0.3	0.0	$\begin{pmatrix} 0.00 & 0 & 0 \\ 0 & 0.70 & -0.36-0.29i \\ 0 & -0.36+0.29i & 0.30 \end{pmatrix}$	$\begin{pmatrix} 0.00 & 0 & 0 \\ 0 & 0.70 & -0.33-0.27i \\ 0 & -0.33+0.27i & 0.30 \end{pmatrix}$	97.19	1.00	0.95
3	0.3	0.3	$\begin{pmatrix} 0.09 & 0 & 0 \\ 0 & 0.70 & -0.12-0.37i \\ 0 & -0.12+0.37i & 0.21 \end{pmatrix}$	$\begin{pmatrix} 0.09 & 0 & 0 \\ 0 & 0.70 & -0.09-0.36i \\ 0 & -0.09+0.36i & 0.21 \end{pmatrix}$	98.73	0.84	0.81
4	0.3	0.5	$\begin{pmatrix} 0.15 & 0 & 0 \\ 0 & 0.70 & -0.03-0.32i \\ 0 & -0.03+0.32i & 0.15 \end{pmatrix}$	$\begin{pmatrix} 0.15 & 0 & 0 \\ 0 & 0.70 & -0.01-0.31i \\ 0 & -0.01+0.31i & 0.15 \end{pmatrix}$	99.33	0.74	0.73
5	0.3	0.7	$\begin{pmatrix} 0.21 & 0 & 0 \\ 0 & 0.70 & 0.03-0.25i \\ 0 & 0.03+0.25i & 0.09 \end{pmatrix}$	$\begin{pmatrix} 0.22 & 0 & 0 \\ 0 & 0.70 & 0.05-0.24i \\ 0 & 0.05+0.24i & 0.08 \end{pmatrix}$	99.69	0.67	0.66
6	0.3	1.0	$\begin{pmatrix} 0.30 & 0 & 0 \\ 0 & 0.70 & 0.00-0.00i \\ 0 & 0.00+0.00i & 0.00 \end{pmatrix}$	$\begin{pmatrix} 0.31 & 0 & 0 \\ 0 & 0.69 & -0.02+0.03i \\ 0 & -0.02-0.03i & 0.00 \end{pmatrix}$	99.71	0.58	0.57
7	0.7	0.0	$\begin{pmatrix} 0.00 & 0 & 0 \\ 0 & 0.30 & -0.36-0.29i \\ 0 & -0.36+0.29i & 0.70 \end{pmatrix}$	$\begin{pmatrix} 0.00 & 0 & 0 \\ 0 & 0.31 & -0.29-0.29i \\ 0 & -0.29+0.29i & 0.69 \end{pmatrix}$	94.92	1.00	0.91
8	0.7	0.3	$\begin{pmatrix} 0.21 & 0 & 0 \\ 0 & 0.30 & -0.12-0.37i \\ 0 & -0.12+0.37i & 0.49 \end{pmatrix}$	$\begin{pmatrix} 0.21 & 0 & 0 \\ 0 & 0.31 & -0.06-0.36i \\ 0 & -0.06+0.36i & 0.48 \end{pmatrix}$	97.75	0.67	0.64
9	0.7	0.5	$\begin{pmatrix} 0.35 & 0 & 0 \\ 0 & 0.30 & -0.03-0.32i \\ 0 & -0.03+0.32i & 0.35 \end{pmatrix}$	$\begin{pmatrix} 0.35 & 0 & 0 \\ 0 & 0.31 & 0.02-0.32i \\ 0 & 0.02+0.32i & 0.34 \end{pmatrix}$	99.20	0.55	0.54
10	0.7	0.7	$\begin{pmatrix} 0.49 & 0 & 0 \\ 0 & 0.30 & 0.03-0.25i \\ 0 & 0.03+0.25i & 0.21 \end{pmatrix}$	$\begin{pmatrix} 0.49 & 0 & 0 \\ 0 & 0.30 & 0.06-0.24i \\ 0 & 0.06+0.24i & 0.21 \end{pmatrix}$	99.68	0.50	0.50
11	0.7	1.0	$\begin{pmatrix} 0.70 & 0 & 0 \\ 0 & 0.30 & 0.00-0.00i \\ 0 & 0.00+0.00i & 0.00 \end{pmatrix}$	$\begin{pmatrix} 0.71 & 0 & 0 \\ 0 & 0.29 & -0.01+0.03i \\ 0 & -0.01-0.03i & 0.00 \end{pmatrix}$	99.63	0.58	0.59
12	1.0	0.0	$\begin{pmatrix} 0.00 & 0 & 0 \\ 0 & 0.00 & -0.00-0.00i \\ 0 & -0.00+0.00i & 1.00 \end{pmatrix}$	$\begin{pmatrix} 0.00 & 0 & 0 \\ 0 & 0.01 & 0.04-0.09i \\ 0 & 0.04+0.09i & 0.98 \end{pmatrix}$	98.45	1.00	0.99
13	1.0	0.3	$\begin{pmatrix} 0.30 & 0 & 0 \\ 0 & 0.00 & -0.00-0.00i \\ 0 & -0.00+0.00i & 0.70 \end{pmatrix}$	$\begin{pmatrix} 0.29 & 0 & 0 \\ 0 & 0.01 & 0.06-0.06i \\ 0 & 0.06+0.06i & 0.70 \end{pmatrix}$	98.87	0.58	0.59
14	1.0	0.5	$\begin{pmatrix} 0.50 & 0 & 0 \\ 0 & 0.00 & -0.00-0.00i \\ 0 & -0.00+0.00i & 0.50 \end{pmatrix}$	$\begin{pmatrix} 0.49 & 0 & 0 \\ 0 & 0.01 & 0.05-0.04i \\ 0 & 0.05+0.04i & 0.50 \end{pmatrix}$	99.07	0.50	0.50
15	1.0	0.7	$\begin{pmatrix} 0.70 & 0 & 0 \\ 0 & 0.00 & 0.00-0.00i \\ 0 & 0.00+0.00i & 0.30 \end{pmatrix}$	$\begin{pmatrix} 0.70 & 0 & 0 \\ 0 & 0.01 & 0.04-0.02i \\ 0 & 0.04+0.02i & 0.29 \end{pmatrix}$	99.24	0.58	0.58
16	1.0	1.0	$\begin{pmatrix} 1.00 & 0 & 0 \\ 0 & 0.00 & 0.00-0.00i \\ 0 & 0.00+0.00i & 0.00 \end{pmatrix}$	$\begin{pmatrix} 0.99 & 0 & 0 \\ 0 & 0.01 & 0.00-0.00i \\ 0 & 0.00+0.00i & 0.00 \end{pmatrix}$	99.05	1.00	0.98

Table I. **Tomography of the output states.** The results are obtained for several combinations of input states (determined by $\lvert\beta\rvert^2$) and reflectivity R of the Mach-Zehnder. All the measurement are in excellent agreement with the theoretical values, showing an average fidelity $F = 98.7\%$, and showing that no additional decoherence is significantly introduced by our device.

network $\vec{q} \in \mathbb{R}^W$ as:

$$s(\vec{x}) = \sum_i^W \frac{\exp(q_i)}{\sum_j \exp(q_j)} \vec{e}_i, \qquad (23)$$

and is only needed to map such output into a human-readable probability vector. The final output of the classifier is considered to be the largest of these probability values. No additional computational power comes from this nonlinear map as it is simply a function on the final output vector of the neural network.

Image classification by sequential data analysis. The first task discussed was a classical image classification problem. Both the training and testing sets consist of images of handwritten digits zero, three and eight, which are chosen for their similarity [8, 9]. Each image is composed of 18×12 pixels whose columns serve as the input to the quantum reservoir, encoded using the above amplitude encoding for each column and then sequentially fed into the network using a finite number of samples. Generally a thousand instances for each encoded state was found to be sufficient to gather approximately correct statistics, yielding the aforementioned 95% accuracy.

For comparing the cases of quantum and classical reservoir computing we have chosen as strategy to keep the topology fixed (meaning optics and readout layer). This allows to switch between the quantum and classical cases by only varying a) how the data is encoded and b) how the reservoir's output is measured. The quantum case is explained above and we give a brief description of the classical simulation here. Instead of encoding data into quantum states, we use finitely bound coherent states that tend to the classical limit.

For input data assumed to be a real vector $\vec{v} \in \mathbb{R}^n$ of length n, we define a set of n coherent states as

$$|\psi_k\rangle = e^{-\frac{k^2}{2}} \sum_n^d \frac{k^n}{\sqrt{n!}} |n\rangle, \qquad (24)$$

on an underlying d-dimensional Fock space (taking a finite truncation of the normally infinite series). This gives a list of n encoding input states that we form a statistical mixture of as $c_i = C_i \sum_j v_j |\psi_j\rangle\langle\psi_j|$, C_i being a normalisation constant such that $\mathrm{tr}[c_i]$ is unity. This classical mixture $c_i \in \mathbb{B}(\mathcal{H}_d)$ serves as the 'classically' encoded input state, sequenced the same as it is for the quantum case. After propagation through the quantum reservoir, projective measurements are performed similar to the quantum case a discrete number of times to produce a sample probability that is then used to update the quantum memristor, ready for the next encoded state of the input sequence. We then see a considerable drop in the overall classification performance, thus giving strong evidence that the performance we are seeing is due to quantum effects.

Furthermore, disabling the quantum memristor's update ability for the original scheme (with single photons) leads to a complete failure. This is unsurprising given that in this case the network must essentially classify the digit with only the very last column to work with - one that very often contains no significant information about the image.

Entanglement detection. The second task considered was entanglement detection, where we require both, random entangled and separable pure states with respect to a bipartition on $\mathcal{H}_d \otimes \mathcal{H}_d$ for training, where $\mathcal{H}_d$ is the d-dimensional complex Hilbert space of the quantum reservoir. This is easily achievable as one can show that separable states are measure zero on the underlying set and so uniform random sampling over $\mathcal{H}_d \otimes \mathcal{H}_d$ will almost surely generate states belonging to the entangled class. For the non-entangled states we randomly sample two quantum states on $\mathcal{H}_d$ and compute their tensor product. Embedding these states into the larger input space of the quantum reservoir, the task is to identify if the input contains any entanglement with respect to the chosen bipartition, yielding the aforementioned 98% success rate on never before seen states.

The code for both tasks is available at [10].

I. Quantum memristor for path-encoded photons

A quantum memristor in the photonic domain was first proposed by Sanz et al. [11]. Although setting an excellent groundwork, their scheme suffers from several drawbacks, most of which can be traced down to the choice of the x-quadrature operator as input variable of the device.

In the example with Fock states — which is arguably the most relevant for quantum photonics applications — they obtain a hysteresis figure that is not pinched at the origin. This has been shown to be possible in memristive devices [12] if the function $f()$ from Eq. (1) goes to infinity, but it is clearly not the case in the device of Sanz et al. [11]. The reason why their device does not obtain a pinched shape hysteresis is that it does not match the form prescribed by Eq. (1), where the input u is required to multiply $f()$. Physically, this happens because an input state with zero quadrature does not always imply an output state with zero photons. Therefore, even though their device clearly shows a memory behaviour, it is not consistent with the definition of *memristive* device.

Most importantly, however, their scheme is very challenging to implement practically, as it requires the tuning and measurement of quadrature operators, which generally entails mixing the states with a coherent beam, thus greatly complicating any experimental setup. Furthermore, the input states are given by the superposition of Fock states, which is possible but impractical to realise in linear optics, especially when considering that the average quadrature of such a state depends on its relative phase term, which would have to be tightly controlled. An additional challenge is the fact that any subsequent manipulation of a qubit encoded in a superposition with the vacuum state would be highly nontrivial.

Nevertheless, the paper by Sanz et al. does make an excellent point by highlighting that performing single-photon detection at one output of the beam splitter not only can be used in conjunction with classical feedback to produce a memory behaviour, but also has the effect of projecting the output on a coherent superposition of quantum states. Starting from this concept, we propose here a solution that substantially improves upon their scheme.

First, we use photon number as the input variable, rather

than the quadrature. This is possible through a close formal analogy that we discovered between the equations of the beam splitter and the equations of Struckov's memristor [13], which we discuss in Supplementary Information J. In addition to producing a hysteresis loop that always crosses the origin, using photon number as input variable allows us to drop the requirement of tuning and measuring quadrature operators, thus greatly simplifying the experimental footprint.

Second, we address the challenge of creating and controlling superposition of Fock states by using a different encoding. In essence, we switch from number-encoding (also referred to as single-rail) to path-encoding, which is perhaps the most natural form of encoding in quantum photonics. The equivalence of the scheme is explained in details in Supplementary Information B.

J. From the "original" memristor to a photonic memristor

After being forgotten for several decades, the memristor had an explosive comeback in 2008 when Struckov et al. [13] reported for the first time a physical model of the "missing memristor" in a simple semiconductor junction. They considered a nanometric junction between a doped semiconductor with resistivity R_{low} and thickness w, and an instrinsic semiconductor with resistivity R_{high} and thickness $D - w$, as represented in Fig. 9. The overall resistance of the junction is easily calculated as the series of its two parts. However, when a voltage is applied to the junction it causes the ions of the doped part to drift, thus effectively changing the resistance of the junction itself. This can be modelled as a shift of w, so that the behaviour of this device can be described by the coupled equations

$$v(t) = \left[R_{\text{low}} \frac{w(t)}{D} + R_{\text{high}} \left(1 - \frac{w(t)}{D} \right) \right] \cdot i(t), \quad (25)$$

$$\dot{w}(t) = \mu \frac{R_{\text{high}}}{D} \cdot i(t), \quad (26)$$

where μ is a constant related to the mobility of the ions inside the semiconductor. One can immediately see that these equations satisfy the form required by Eqs. (1) and (2). Abstractly, one can think of this device as a sort of sliding potentiometer where the position of the slider $w(t)$ — i.e. the state variable of the device — is influenced by the past current that went through the device, hence the hysteresis.

Let us now consider the tunable beam splitter of Fig. 10a. In an idealized picture, one has the elementary relation

$$\langle n_{\text{out}} \rangle = (1 - R(\theta)) \langle n_{\text{in}} \rangle, \quad (3)$$

where $R(\theta) = [0, 1]$. In a real-world device, however, the reflectivity can never reach *exactly* zero or one. That is because, even if one assumes a lossless device, a fraction of the input light (however small) will always leak into the undesired output arm. This is especially true in integrated optics, where a common way to realise a tunable beam splitter is by a Mach-Zehnder interferometer with a phase shifter in one of the arms, as shown in Fig. 10b. If the two directional couplers composing the Mach-Zehnder have a perfectly balanced
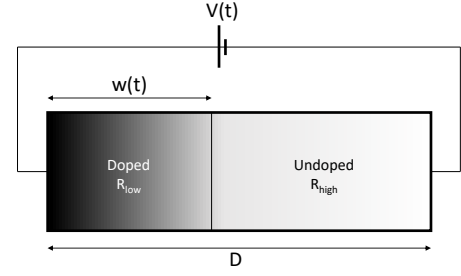

Figure 9. **Original memristor by Struckov et al [13].** When a voltage is applied across the junction, the ideal separation line between doped and undoped semiconductor shifts, thereby changing the resistance of the junction itself, and originating the hysteresis.
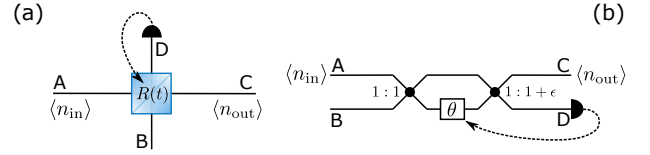

Figure 10. **Photonic quantum memristor.** a) Basic scheme of the photonic quantum memristor. b) The integrated optics equivalent, where the reflectivity is set by the phase θ. The black lines correspond to guided modes of the integrated chip, and the crossing points are directional couplers, which act as beam splitters.

splitting ratio of 1:1, the device has the ideal operation of Eq. (3). In practice, however, the exact splitting ratio can only be achieved up to a given experimental accuracy. Let us then consider a Mach-Zehnder where, for simplicity, one of the couplers is assumed to be perfectly balanced and the other to be slightly off. In the Heisenberg picture, the action of the Mach-Zehnder can be described by the matrix product of its three components:

$$\begin{pmatrix} \hat{a}_C \\ \hat{a}_D \end{pmatrix} = \begin{pmatrix} t & ir \\ ir & t \end{pmatrix} \begin{pmatrix} 1 & 0 \\ 0 & e^{i\theta} \end{pmatrix} \frac{1}{\sqrt{2}} \begin{pmatrix} 1 & i \\ i & 1 \end{pmatrix} \begin{pmatrix} \hat{a}_A \\ \hat{a}_B \end{pmatrix}, \quad (27)$$

where $\hat{a}$ is the annihilation operator on each spatial mode and the three matrices from left to right refer to the action of the unbalanced directional coupler, the phase shifter and the balanced coupler, respectively. Here, r and t indicate the reflection and transmission coefficients of the unbalanced coupler. By computing the product one obtains

$$\begin{pmatrix} \hat{a}_C \\ \hat{a}_D \end{pmatrix} = \frac{1}{\sqrt{2}} \begin{pmatrix} t - re^{i\theta} & i(t + re^{i\theta}) \\ i(t + re^{i\theta}) & -r + te^{i\theta} \end{pmatrix} \begin{pmatrix} \hat{a}_A \\ \hat{a}_B \end{pmatrix}. \quad (28)$$

In analogy with the beam splitter of Fig. 10a, let us consider A as input port and C as output port, while input B is not used. One can extract from the previous matrix

$$\hat{a}_C = \frac{1}{\sqrt{2}} (t - re^{i\theta}) \hat{a}_A, \quad (29)$$

from which we obtain

$$\langle n_{\text{out}} \rangle = \frac{1}{2} (1 - 2rt \cos\theta) \langle n_{\text{in}} \rangle. \quad (30)$$

In the ideal case, when $r = t = 1/\sqrt{2}$, the equation reduces to the well known

$$\langle n_{\text{out}} \rangle = \frac{1}{2}(1 - \cos\theta)\langle n_{\text{in}} \rangle, \tag{31}$$

and by comparison with Eq. (3) one easily finds

$$R(\theta) = \frac{1}{2}(1 + \cos\theta). \tag{32}$$

Because of the relation $r^2 + t^2 = 1$, the product rt in Eq. (30) takes its maximum value of $1/2$ for $r = 1/\sqrt{2}$. In a more realistic picture, where r can only approximate the ideal value, one has $rt = 1/2 - \eta$ with $\eta \ll 1$. Introducing this product in Eq. (30) one obtains

$$\langle n_{\text{out}} \rangle = \frac{1}{2}(1 - (1 - 2\eta)\cos\theta)\langle n_{\text{in}} \rangle. \tag{33}$$

By the definition of Eq. (32) and some simple algebra, one can rewrite the last equation as

$$\langle n_{\text{out}} \rangle = \left[\eta R(\theta) + (1 - \eta)(1 - R(\theta))\right]\langle n_{\text{in}} \rangle, \tag{34}$$

which is our final point. This equation is a reasonable representation of a real-world beam splitter, for which the transmission never reaches exactly zero or one. Indeed, one can only control $R(\theta)$, and for $R(\theta) = 0$ the transmission is $1 - \eta$, while for $R(\theta) = 1$ the transmission is η. We call η a *leakage factor*, as it represents the fraction of photons that, regardless of the external control, always leaks into the undesired output.

At this point, we observe that Eq. (34) is formally identical to Eq. (25), where $\langle n_{\text{in}} \rangle$ corresponds to $i(t)$, $\langle n_{\text{out}} \rangle$ corresponds to $v(t)$, η corresponds to R_{low}, $1 - \eta$ corresponds to R_{high}, and $R(\theta)$ corresponds to $w(t)/D$, both of them being adimensional quantities in the interval $[0, 1]$ and acting as state variables for the respective device. We also emphasise that the analogy does not break down when considering an ideal beam splitter with $\eta = 0$, as it just corresponds to an ideal memristor with $R_{\text{low}} = 0$. This is nearly the case in reality, as the resistance of doped semiconductors is tipically many orders of magnitude smaller than intrinsic semiconductors, even at moderate doping.

We have then found in the beam splitter a device that inherently replicates the form of Eq. (25). Consequently, the natural choice of the feedback law would be one that replicates the dynamics of Eq. (26). By the mere correspondence of the quantities, this would translate to $\dot{R}(\theta) \propto \langle n_{\text{in}} \rangle$. However, a feedback law of this type would be rather pointless because, unlike current and voltage, photon number can only take positive values and therefore $R(\theta)$ would just increase in time, eventually saturating to unity. One of the fundamental properties of a memristor, instead, is the ability to revert its state, which implies that $\dot{R}(\theta)$ must also take negative values. This can be readily obtained by a simple baseline shift:

$$\dot{R}(\theta, t) = \langle n_{\text{in}}(t) \rangle - 0.5\langle n \rangle_{\text{max}}, \tag{4}$$

where $\langle n \rangle_{\text{max}}$ is the maximum value of $\langle n_{\text{in}} \rangle$ in time. In the single-photon case, $\langle n_{\text{max}} \rangle = 1$, so the law effectively becomes $\dot{R}(\theta) = \langle n_{\text{in}} \rangle - 0.5$. It is easy to see that in such a case, input states with average number of photons lower than 0.5 will contribute negatively and bring R to zero, while input states with average number of photons higher than 0.5 will contribute positively and bring R to one. The resulting dynamics is an hysteresis figure that closely resembles that of the original memristor, though limited to the positive quadrant of the input-output plane.

[1] Francesco Ceccarelli, Simone Atzeni, Ciro Pentangelo, Francesco Pellegatta, Andrea Crespi, and Roberto Osellame, "Low power reconfigurability and reduced crosstalk in integrated photonic circuits fabricated by femtosecond laser micromachining," Laser & Photonics Reviews **14**, 2000024 (2020).

[2] Giacomo Corrielli, Simone Atzeni, Simone Piacentini, Ioannis Pitsios, Andrea Crespi, and Roberto Osellame, "Symmetric polarization-insensitive directional couplers fabricated by femtosecond laser writing," Optics express **26**, 15101–15109 (2018).

[3] Yan Li and Shiliang Qu, "Water-assisted femtosecond laser ablation for fabricating three-dimensional microfluidic chips," Current Applied Physics **13**, 1292–1295 (2013).

[4] Reo Murakami, Hiroyuki Nakagawa, and Shigeki Matsuo, "Water-assisted laser drilling for miniature internal thread in glass and evaluation of its strength," Journal of Laser Micro Nanoengineering **12**, 203–206 (2017).

[5] Francesco Ceccarelli, Simone Atzeni, Alessandro Prencipe, Raffaele Farinaro, and Roberto Osellame, "Thermal phase shifters for femtosecond laser written photonic integrated circuits," Journal of Lightwave Technology **37**, 4275–4281

(2019).

[6] Leon O Chua and Sung Mo Kang, "Memristive devices and systems," Proceedings of the IEEE **64**, 209–223 (1976).

[7] Felix A. Pollock, César Rodríguez-Rosario, Thomas Frauenheim, Mauro Paternostro, and Kavan Modi, "Non-markovian quantum processes: Complete framework and efficient characterization," Phys. Rev. A **97**, 012127 (2018).

[8] Yann LeCun, Corinna Cortes, and CJ Burges, "Mnist handwritten digit database," ATT Labs [Online]. Available: http://yann.lecun.com/exdb/mnist **2** (2010).

[9] Martín Abadi, Ashish Agarwal, Paul Barham, Eugene Brevdo, Zhifeng Chen, Craig Citro, Greg S. Corrado, Andy Davis, Jeffrey Dean, Matthieu Devin, Sanjay Ghemawat, Ian Goodfellow, Andrew Harp, Geoffrey Irving, Michael Isard, Yangqing Jia, Rafal Jozefowicz, Lukasz Kaiser, Manjunath Kudlur, Josh Levenberg, Dan Mané, Rajat Monga, Sherry Moore, Derek Murray, Chris Olah, Mike Schuster, Jonathon Shlens, Benoit Steiner, Ilya Sutskever, Kunal Talwar, Paul Tucker, Vincent Vanhoucke, Vijay Vasudevan, Fernanda Viégas, Oriol Vinyals, Pete Warden, Martin Wattenberg, Martin Wicke, Yuan Yu, and Xiaoqiang Zheng, "TensorFlow: Large-scale machine learning

on heterogeneous systems," (2015), software available from tensorflow.org.

[10] J. Morris, "Quantum memristors," https://github.com/QCmonk/Qmemristor (2021).

[11] Mikel Sanz, Lucas Lamata, and Enrique Solano, "Invited article: Quantum memristors in quantum photonics," APL Photonics **3**, 080801 (2018).

[12] Massimiliano Di Ventra and Yuriy V Pershin, "On the physical properties of memristive, memcapacitive and meminductive systems," Nanotechnology **24**, 255201 (2013).

[13] Dmitri B Strukov, Gregory S Snider, Duncan R Stewart, and R Stanley Williams, "The missing memristor found," nature **453**, 80–83 (2008).